

# Analyst

Accepted Manuscript



This is an *Accepted Manuscript*, which has been through the Royal Society of Chemistry peer review process and has been accepted for publication.

*Accepted Manuscripts* are published online shortly after acceptance, before technical editing, formatting and proof reading. Using this free service, authors can make their results available to the community, in citable form, before we publish the edited article. We will replace this *Accepted Manuscript* with the edited and formatted *Advance Article* as soon as it is available.

You can find more information about *Accepted Manuscripts* in the [Information for Authors](#).

Please note that technical editing may introduce minor changes to the text and/or graphics, which may alter content. The journal's standard [Terms & Conditions](#) and the [Ethical guidelines](#) still apply. In no event shall the Royal Society of Chemistry be held responsible for any errors or omissions in this *Accepted Manuscript* or any consequences arising from the use of any information it contains.

1  
2  
3  
4  
5  
6  
7  
8  
9  
10  
11  
12  
13  
14  
15  
16  
17  
18  
19  
20  
21  
22  
23  
24  
25  
26  
27  
28  
29  
30  
31  
32  
33  
34  
35  
36  
37  
38  
39  
40  
41  
42  
43  
44  
45  
46  
47  
48  
49  
50  
51  
52  
53  
54  
55  
56  
57  
58  
59  
60

## Surface Charge, Electroosmotic Flow and DNA Extension in Chemically Modified Thermoplastic Nanoslits and Nanochannels

Franklin I. Uba,<sup>1,6</sup> Swathi R. Pullagurla,<sup>3</sup> Nichanun Sirasunthorn,<sup>5</sup> Jiahao Wu,<sup>4</sup> Sunggook Park,<sup>4</sup> Rattikan Chantiwas,<sup>5</sup> Yoonkyoung Cho,<sup>6</sup> Heungjoo Shin<sup>6</sup> and Steven A. Soper<sup>1,2,6\*</sup>

<sup>1</sup>Department of Chemistry, UNC-Chapel Hill, NC, 27599

<sup>2</sup>Department of Biomedical Engineering, UNC-Chapel Hill, NCSU, Raleigh, NC

<sup>3</sup>Department of Chemistry, Louisiana State University, Baton-Rouge, LA, 70803

<sup>4</sup>Department of Mechanical Engineering, Louisiana State University, Baton-Rouge, LA

<sup>5</sup>Department of Chemistry and Center of Excellence for Innovation in Chemistry, Faculty of Science, Mahidol University, Bangkok, Thailand

<sup>6</sup>Ulsan National Institute of Science and Technology, South Korea

\*corresponding author [ssoper@unc.edu](mailto:ssoper@unc.edu)

**ABSTRACT**

Thermoplastics have become attractive alternatives to glass/quartz for microfluidics, but the realization of thermoplastic nanofluidic devices has been slow in spite of the rather simple fabrication techniques that can be used to produce these devices. This slow transition has in part been attributed to insufficient understanding of surface charge effects on the transport properties of single molecules through thermoplastic nanochannels. We report the surface modification of thermoplastic nanochannels and an assessment of the associated surface charge density, zeta potential and electroosmotic flow (EOF). Mixed-scale fluidic networks were fabricated in poly(methylmethacrylate), PMMA. Oxygen plasma was used to generate surface-confined carboxylic acids with devices assembled using low temperature fusion bonding. Amination of the carboxylated surfaces using ethylenediamine (EDA) was accomplished via EDC coupling. XPS and ATR-FTIR revealed the presence of carboxyl and amine groups on the appropriately prepared surfaces. A modified conductance equation for nanochannels was developed to determine their surface conductance and was found to be in good agreement with our experimental results. The measured surface charge density and zeta potential of these devices were lower than glass nanofluidic devices and dependent on the surface modification adopted, as well as the size of the channel. This property, coupled to an apparent increase in fluid viscosity due to nanoconfinement, contributed to the suppression of the EOF in PMMA nanofluidic devices by an order of magnitude compared to the micro-scale devices. Carboxylated PMMA nanochannels were efficient for the transport and elongation of  $\lambda$ -DNA while these same DNA molecules were unable to translocate through aminated nanochannels.

**Keywords:** Nanofluidics, Thermoplastics, Surface Modification, Surface Charge, DNA Extension, Electroosmotic Flow

1  
2  
3 Fluidic channels with one or two dimensions in the nanometer scale, nanoslits or nanochannels,  
4  
5 respectively, have generated great interest because of unique phenomena that occurs in nano-  
6  
7 confined space such as nanocapillarity,<sup>1</sup> concentration polarization<sup>2,3</sup> and electrical double layer  
8  
9 (EDL) overlap.<sup>4-7</sup> These properties arise when the channel size is comparable to either the length  
10  
11 scales of electrostatic interactions in solution or the size of the molecules being transported  
12  
13 through them. Some of the interesting applications that arise from the use of nanochannels  
14  
15 include single-molecule analysis,<sup>8-11</sup> molecular pre-concentration,<sup>12</sup> chemical analyses of mass-  
16  
17 limited samples,<sup>13, 14</sup> DNA electrophoresis,<sup>15-17</sup> desalination,<sup>18</sup> nanofluidic diodes,<sup>19</sup> real-time  
18  
19 probing of biomolecules,<sup>20-24</sup> ionic transport,<sup>25</sup> and entropic trapping for DNA  
20  
21 separations.<sup>26</sup> Controlled fabrication of nanochannels has facilitated the study of charge-based  
22  
23 phenomena like ion enrichment and depletion and surface-charge-governed transport.<sup>27-29</sup>  
24  
25  
26  
27  
28

29 As described by Chantiwas *et al.*,<sup>30</sup> thermoplastic nanofluidic devices offer an attractive  
30  
31 alternative to glass/quartz devices due to the materials' diverse physiochemical properties and  
32  
33 the fabrication techniques available to design the prerequisite structures. A commonly employed  
34  
35 modality for the fabrication of thermoplastic nanofluidic devices is nanoimprint lithography  
36  
37 (NIL).<sup>31-34</sup> This technique takes advantage of the deformability of the substrate at temperatures  
38  
39 above the glass transition temperature (T<sub>g</sub>) of the substrate to produce multi-scale structures in a  
40  
41 relatively high production mode over large areas at moderate cost.<sup>35</sup>  
42  
43  
44  
45

46 Another benefit of using thermoplastics for nanofluidics is the diversity in their surface  
47  
48 chemistry, which is determined by the identity of the monomer units comprising the polymer  
49  
50 chains such as poly(methylmethacrylate), PMMA, containing methyl ester monomer units. In  
51  
52 addition, a diverse range of simple activation techniques can be employed to generate functional  
53  
54 groups that alter the surface chemistry.<sup>36-40</sup> Common surface activation protocols for polymer  
55  
56  
57  
58  
59  
60

1  
2  
3 fluidic devices are ultraviolet (UV) and plasma activation.<sup>41-43</sup> These activation techniques have  
4  
5 been reported to generate a host of surface oxygen-containing species, such as carbonyls  
6  
7 (aldehydes, ketones and carboxylic acids) and alcohols following a sequence of free-radical  
8  
9 photo-initiated oxidation reactions.<sup>42,44</sup>  
10  
11

12  
13 Surface activation of polymer substrates possessing nanofluidic structures requires careful  
14  
15 control of the dose to minimize activation-induced nano-scale roughness that may affect the  
16  
17 operational characteristics of the device.<sup>45</sup> Plasma treatment has been the method of choice for  
18  
19 nanofluidic surface activation and low-temperature assembly of nanofluidic devices as it induces  
20  
21 minimal surface root-mean-square (RMS) roughness, lacks diffraction limitations and shadowing  
22  
23 effects as reported for UV activation of polymer microchannels,<sup>39</sup> and allows for low  
24  
25 temperature assembly of the device to maintain surface functionality and minimize nanostructure  
26  
27 deformation.<sup>34</sup> Exposing PMMA to controlled O<sub>2</sub> plasma conditions can generate surface  
28  
29 carboxylic acids,<sup>42</sup> which remain accessible for subsequent modification reactions after device  
30  
31 thermal assembly.  
32  
33  
34  
35

36  
37 In a previous work, we reported the generation of positively charged surfaces in PMMA  
38  
39 microchannels following both chemical (*N*-lithiodiaminoethane reaction)<sup>40</sup> and photochemical  
40  
41 (UV) pathways.<sup>38</sup> To the best of our knowledge, most of the work on nanochannel surface  
42  
43 modification has involved functionalization of surface silanol groups in glass or fused silica,<sup>28</sup>  
44  
45 particularly for the immobilization of biomolecules.<sup>25, 29, 46</sup> Glass possesses well-established  
46  
47 surface chemistry, hydrophilicity, non-conductivity, rigidity, minimal surface defects, non-  
48  
49 deformability at high pressures and well-established top-down fabrication techniques.<sup>47, 48</sup>  
50  
51 However, with the growing interests in elastomeric,<sup>49-52</sup> thermoplastic<sup>32</sup> and membrane-based<sup>53,</sup>  
52  
53  
54  
55  
56  
57  
58  
59  
60  
<sup>54</sup> nanofluidic devices, it becomes necessary to understand the effects of surface modification on

1  
2  
3 the charge density and surface charge-governed transport in thermoplastic nanofluidic channels,  
4 especially when considering such devices for many of the applications discussed previously.<sup>28, 55</sup>  
5  
6  
7

8 In this work, we report the surface modification of thermoplastic nanoslits and nanochannels  
9 and the determination of the surface charge density, zeta potential and electroosmotic flow  
10 (EOF) in these devices. The nanofluidic devices were fabricated in PMMA using a simplified  
11 protocol that did not require UV or thermal NIL, significantly simplifying the production of  
12 devices, even for devices with structures to ~20 nm. Carboxyl groups were generated on the  
13 walls of PMMA nanoslits and nanochannels under controlled conditions, including the plasma  
14 exposure time and oxygen gas flow rate.<sup>42, 44</sup> The surface-confined carboxyl groups were  
15 subsequently aminated by reaction with a solution of ethylenediamine (EDA). The extent of  
16 roughness induced by surface activation was assessed in a nanoslit device using atomic force  
17 microscopy (AFM). Surface conductance plots were generated for the fluidic devices using a  
18 range of KCl concentrations. In agreement with our measurements, a modified model of ion  
19 transport in nanofluidic devices based on Schoch *et al.*<sup>55</sup> was presented. In addition, we  
20 investigated the effects of solution pH on the surface charge density and the EOF and assessed  
21 the ability of these devices for DNA translocation.  
22  
23  
24  
25  
26  
27  
28  
29  
30  
31  
32  
33  
34  
35  
36  
37  
38  
39  
40  
41

## 42 **EXPERIMENTAL METHODS**

43  
44 **Materials and reagents.** PMMA sheets and cover plates were purchased from Good Fellow  
45 (Berwyn, PA), Cyclic olefin copolymer (COC 6017) was purchased from TOPAS Advanced  
46 Polymers (Florence KY) and Si <100> wafers were purchased from University Wafers (Boston,  
47 MA). Isopropanol, 1-ethyl-3-[dimethylaminopropyl] carbodimide hydrochloride (EDC), 2-(4-  
48 morpholino)-ethane sulfonic acid (MES), ethylenediamine (EDA), tripropylene glycol diacrylate  
49 (TPGA), trimethylolpropane triacrylate (TMPA), Irgacure 651 (photo-initiator), 50% potassium  
50  
51  
52  
53  
54  
55  
56  
57  
58  
59  
60

1  
2  
3 hydroxide (KOH), hydrochloric acid (HCl) and potassium chloride (KCl) were obtained from  
4 Sigma-Aldrich (St. Louis, MO). An anti-adhesion monolayer of (tridecafluoro – 1,1,2,2 –  
5 tetrahydrooctyl) trichlorosilane (T-silane) was purchased from Gelest, Inc. Tris buffer (pH =  
6 8.0) and 2-(*N*-morpholino)ethanesulfonic acid (MES) buffer (pH 5.0) were obtained from Fisher  
7 Scientific (Houston, TX) and Life Technologies (Carlsbad, CA), respectively. All required  
8 dilutions were performed using 18 MΩ/cm milliQ water (Millipore) and buffer solutions were  
9 filtered using a 0.2 μm filter.  
10  
11

12  
13 **Fabrication of nanofluidic devices.** Device fabrication involved four steps. First, a Si master  
14 was developed by initially patterning two V-shaped access microfluidic channels, 55 μm wide,  
15 12 μm deep and 1.5 cm long in a Si <100> wafer using standard photolithography and  
16 anisotropic etching with 50% KOH. Next, the nanofluidic channels were milled using a Helios  
17 NanoLab 600 DualBeam instrument (FEI) Focused Ion Beam (FIB) instrument. In most cases, a  
18 beam current of 9.7 pA (diameter FWHM of 14 nm at 30 keV Ga<sup>+</sup> ions at normal incidence) and  
19 a dwell time of 1 μs were used to fabricate the desired nanochannels. For nanochannels <50 nm,  
20 an Al film with sputtering yield of 0.30 μm<sup>3</sup>/nC was deposited onto the Si wafer. The type and  
21 thickness of conductive film were chosen based on a previous report.<sup>48</sup> After FIB milling, the Al  
22 layer was removed using an Al etching solution, cleaned with copious amounts of water and  
23 dried with N<sub>2</sub> gas.  
24  
25  
26  
27  
28  
29  
30  
31  
32  
33  
34  
35  
36  
37  
38  
39  
40  
41  
42  
43  
44

45  
46 The patterned Si wafer, which served as the master for producing the resin stamp, was coated  
47 with an anti-adhesion monolayer of T-silane from the gas phase in a desiccator under vacuum for  
48 2 h. The structures were then transferred into a UV-curable resin containing 68 wt% TPGA as  
49 the base, 28 wt% TMPA as a crosslinking agent and 4 wt% Irgacure 651 as photo-initiator that  
50 on a COC backbone. To produce resin stamps with protrusive structures, the Si master was  
51  
52  
53  
54  
55  
56  
57  
58  
59  
60

1  
2  
3 covered with the UV resin by dispensing with a pipette followed by gentle pressing of the COC  
4  
5 plate on the resin-coated master to ensure complete filling of the resin into mold cavities. This  
6  
7 was followed by exposure to a 365 nm UV light ( $10 \text{ J/m}^2$ ) through the COC plate for 5 min in a  
8  
9 CL-100 Ultraviolet crosslinker. After curing, the UV-curable resin was gently demolded from  
10  
11 the Si master.  
12  
13

14  
15 The patterned UV-curable resin was used as the stamp to hot emboss structures into a 1.5  
16  
17 mm-thick PMMA sheet with access holes for reservoirs drilled prior or after embossing.  
18  
19 Embossing was performed using a Hex03 hot embosser (JenOptik) at a pressure of  $1910 \text{ kN/m}^2$   
20  
21 for 120 s with the top and bottom plates maintained at a temperature of  $125^\circ\text{C}$ . The pressure was  
22  
23 applied after 30 s preheating of the stamp and the substrate at the desired molding temperature  
24  
25 and was maintained during the imprinting process until cooled to  $40^\circ\text{C}$ . After cooling, the  
26  
27 PMMA replica was demolded from the UV-resin stamp.  
28  
29

30  
31 For enclosing the fluidic substrate, a  $175 \mu\text{m}$  thick PMMA sheet was used as a cover plate.  
32  
33 Both the patterned PMMA sheet and cover plate were pre-activated using oxygen plasma at 50  
34  
35 W for 35 s and 5.5 sccm oxygen gas flow rate. Thermal assembly was performed at  $80^\circ\text{C}$  for 400  
36  
37 s at a pressure of  $370 \text{ kN/m}^2$ .  
38  
39

40  
41 **Surface modification.** Surface amination reactions were initially tested on planar PMMA  
42  
43 substrates ( $1 \text{ cm} \times 1 \text{ cm}$ ). PMMA substrates were exposed to 50 W (5.5 sccm)  $\text{O}_2$  plasma for 35 s  
44  
45 to generate the carboxylic acid functional scaffolds necessary for the amination reaction (Scheme  
46  
47 1). The plasma modified samples were then soaked in 5 ml buffered solution (100 mM MES, pH  
48  
49 5.0) containing 250 mg EDC and 330  $\mu\text{l}$  EDA (density =  $0.899 \text{ g/cm}^3$ ) for 20 min at room  
50  
51 temperature. After incubation, samples were rinsed with deionized water and air dried. The same  
52  
53 protocol was adopted for the amination of assembled PMMA nanofluidic devices containing  
54  
55  
56  
57  
58  
59  
60

1  
2  
3 either nanoslits or nanochannels. In this case, the assembled devices were immediately filled  
4 with the EDA-EDC/MES solution and allowed to incubate for 20 min and rinsed with deionized  
5  
6 water prior to experiments.  
7  
8  
9

10 **Water contact angle and surface energy determinations.** The wettability of unmodified and  
11 modified PMMA surface was assessed by water contact-angle measurements using a VCA  
12  
13 Optima instrument (AST Products). PMMA sheets (1.5 mm thick) were cut to 1 cm × 1 cm and  
14  
15 the surfaces modified as described above. A volume of 2.0 μL nanopure water (18.2MΩ·cm at  
16  
17 25°C) was dispensed onto the substrate and the photograph of each droplet was captured  
18  
19 immediately for analysis using the software provided by the manufacturer. The measurements  
20  
21 were repeated at least five times at separate positions on the substrate and the values reported as  
22  
23 the mean ±one standard deviation. Surface energies of the surfaces were deduced from the  
24  
25 Zisman plot created by measuring the contact angle of a series of liquids with known liquid-  
26  
27 vapor surface tensions ( $\gamma_{lv}$ ). The liquids used were water ( $\gamma_{lv} \sim 72.80 \text{ mJ/m}^2$ ), glycerol ( $\gamma_{lv} \sim$   
28  
29  $64.00 \text{ mJ/m}^2$ ) and DMSO ( $\gamma_{lv} \sim 43.54 \text{ mJ/m}^2$ ) (see SI for more information).  
30  
31  
32  
33  
34  
35

36 **Atomic Force Microscopy (AFM).** The topologies of untreated PMMA (u-PMMA), Plasma  
37 modified PMMA (O<sub>2</sub>-PMMA) and amine modified PMMA (NH<sub>2</sub>-PMMA) planar surfaces and  
38  
39 the bottom surface of nanoslits were investigated using the Asylum Research MFP-3D Atomic  
40  
41 Force Microscope (tip radius ~2 nm) in repulsive tapping mode at a rate of 1.0 Hz. The  
42  
43 Tap300A1-G cantilever tips (Ted Pella) had a frequency of 300 kHz and force constant of 40  
44  
45 N/m. For the planar surfaces, the scans were taken over a 3.5 μm × 3.5 μm scan size and the  
46  
47 RMS surface roughness computed using the manufacturer's software. In the nanoslit, a scan size  
48  
49 of 4 μm × 500 nm was acquired.  
50  
51  
52  
53  
54  
55  
56  
57  
58  
59  
60

1  
2  
3 **Scanning Electron Micrographs (SEMs).** For SEM, the resin stamp and PMMA substrate were  
4 pre-coated with a 2-3 nm Au/Pd layer and imaged under high vacuum with an FEI Quanta 200  
5 field emission gun at a 5 kV accelerating voltage.  
6  
7

8  
9  
10 **Surface charge measurements.** Direct current conductance plots were used to determine the  
11 surface charge of the nanoslits and nanochannel devices. Prior to all measurements, fluidic  
12 devices were flushed with a binary mixture of methanol/ultrapure water (50% v/v). Nanochannel  
13 filling was aided by capillary pulling from the inlet reservoir and vacuum suction from the outlet  
14 reservoir to ensure complete filling and the elimination of air-bubbles. Finally, fluidic channels  
15 were rinsed several times with deionized water before filling with the desired electrolyte.  
16  
17

18  
19  
20 Next, pre-cleaned devices were filled with the KCl solutions and Ag/AgCl electrodes were  
21 immersed into the access reservoirs poised at the ends of microchannels. Electrolyte solutions  
22 were allowed to equilibrate for 3-5 min evidenced by a stable resistance value under a bias  
23 voltage. The conductance values were determined by fitting the slope of the ionic current as a  
24 function of the applied voltage, which was stepped from -1V to 1V with 50 mV step size and a 5  
25 s holding time for each data point. All measurements were achieved with a low noise Axopatch  
26 200B amplifier coupled to a digidata 1440A digitizer with signal acquisition and analysis  
27 performed with the pClamp10 control software. The measurements were performed five times  
28 with repeated draining and filling. The mean conductance was plotted against the electrolyte  
29 concentration in a log-log plot and the surface charge determined from these graphs. This  
30 experiment was also performed with KCl solutions prepared over a pH range of 3.5 to 12 to  
31 investigate the effects of pH on surface charge. The solution pH was adjusted using HCl or  
32 KOH. No pressure difference across the nanochannel was induced during the measurements. To  
33 avoid carry-over errors, each measurement was performed using a new device.  
34  
35  
36  
37  
38  
39  
40  
41  
42  
43  
44  
45  
46  
47  
48  
49  
50  
51  
52  
53  
54  
55  
56  
57  
58  
59  
60

1  
2  
3 **Electroosmotic Flow (EOF).** Two devices, one possessing a single PMMA nanoslit (138  $\mu\text{m}$   
4 long, 50 nm deep and 1  $\mu\text{m}$  wide) and a single nanochannel (138  $\mu\text{m}$  long, 120 nm high and 120  
5 nm wide) connecting two opposite V-shaped access microchannels were fabricated as previously  
6 described. Fluidic channels were activated and the EOF was assessed using the current  
7 monitoring method. EOF values were measured using 0.1 and 0.05 M KCl solutions in 10 mM  
8 Tris buffer at pH 7.8. First, the pre-cleaned primed device was filled with 0.1 M solution and  
9 allowed to equilibrate for 3 min under a 1 V DC bias. Next, one access reservoir was emptied  
10 and 0.05 M KCl was introduced. Ag/AgCl electrodes were placed in the reservoirs across the  
11 channels under a 200 mV DC bias. Signals were acquired using the Axopatch 200B amplifier  
12 with a pClamp10 software and Digidata 1440A digitizer set at 10 kHz sampling frequency.  
13  
14

15  
16  
17 **Transport dynamics of  $\lambda$ -DNA through thermoplastic nanochannels.** To study the  
18 electrokinetic parameters and extension length of  $\lambda$ -DNA, 100  $\times$  100 nm nanochannels were  
19 used.  $\lambda$ -DNA (Promega Corporation) were stained with the bis-intercalating dye, YOYO-1  
20 (Molecular Probes, Eugene, OR) at a base-pair/dye ratio of 5:1 in an electrolyte solution of 1X  
21 TBE (89 mM Tris, 89 mM Borate, 1 mM EDTA) with the addition of 4% v/v  $\beta$ -mercaptoethanol  
22 as a radical scavenger to minimize photo-induced damage (photobleaching and/or photoniccking).  
23 Experiments were performed using 0.75 pM DNA solutions. Fluorescence microscopy was  
24 performed with an inverted microscope (Olympus IX81 TIRF microscope, Olympus,  
25 Pennsylvania, PA) equipped with a 100 $\times$ /1.49 NA oil immersion objective and 488 nm laser  
26 light for excitation and a Sedat laser filter set LF488/561-2X2M-B-000 (Semrock). Images were  
27 acquired at  $\sim$ 150 fps using a Hamamatsu EMCCD digital camera with EM gain and analyzed  
28 using Metamorph software.  
29  
30  
31  
32  
33  
34  
35  
36  
37  
38  
39  
40  
41  
42  
43  
44  
45  
46  
47  
48  
49  
50  
51  
52  
53  
54  
55  
56  
57  
58  
59  
60

1  
2  
3 Buffer solution was initially added into the precleaned chip then the buffer solution in one of  
4 the microchannels was replaced with a solution containing the stained  $\lambda$ -DNA. Lambda DNA  
5 was electrokinetically driven through the nanochannels by immersing platinum electrodes into  
6 reservoirs situated on either side of the nanochannel and applying a DC bias voltage using a  
7 variable voltage power supply.  
8  
9

10  
11 To study the degree of extension of  $\lambda$ -DNA confined in the PMMA nanochannels, the  $\lambda$ -  
12 DNA was initially driven from the microchannel into the nanochannel under a field strength of  
13 100 V/cm. Once the DNA molecule had fully entered the nanochannel, the DC field was  
14 switched off. The molecule was allowed to relax until it reached its equilibrium extension length  
15 inside the channel before an image was acquired at a 50 ms exposure time. The end-to-end  
16 distance of the fluorescence image was measured using ImageJ software and displayed in a  
17 histogram.  
18  
19

## 20 RESULTS AND DISCUSSION

21  
22 **Device fabrication.** The fabrication steps adopted for building the thermoplastic nanofluidic  
23 devices are depicted in Figures 1a – c. This fabrication strategy is a simplified scheme of an NIL  
24 process previously reported in our group.<sup>33</sup> The resin stamp was made by casting the non-cured  
25 UV resin against a Si master and applying pressure to the resin using a COC plate. UV curing  
26 was accomplished with a benchtop UV crosslinking chamber. Thermal embossing was used to  
27 transfer the nanofluidic structures into PMMA from the UV-curable resin stamp and the device  
28 was sealed with a PMMA cover plate using low-temperature plasma assisted bonding to build  
29 the enclosed mixed-scale device (Figure 1c). Shown are SEMs of devices possessing an array of  
30 4 nanoslits (Figure 1d – f) or 7 nanochannels (Figure 1g – i). The nanostructures, which were  
31  
32  
33  
34  
35  
36  
37  
38  
39  
40  
41  
42  
43  
44  
45  
46  
47  
48  
49  
50  
51  
52  
53  
54  
55  
56  
57  
58  
59  
60

1  
2  
3 fabricated by FIB milling into the Si master, were designed with dimensions (width  $\times$  depth) of 1  
4  $\mu\text{m} \times 50 \text{ nm}$  and  $120 \text{ nm} \times 120 \text{ nm}$  for the nanoslits and nanochannels, respectively.<sup>33</sup>  
5  
6  
7

8 This fabrication scheme was also used to produce  $40 \times 40 \text{ nm}$  and approximately  $20 \times 20 \text{ nm}$   
9 nanochannels in PMMA substrates - the smallest reported nanofluidic channel to date fabricated  
10 in a thermoplastic substrate. Figure 1j shows the cross-sectional image of the  $20 \times 20 \text{ nm}$   
11 nanochannel FIB milled into a Si master through an 80 nm thick Al layer after removal of the  
12 conductive layer. The top-view of the channel after transfer into the thermoplastic is shown in  
13 Figures 1k. We observed that the final width and depth of the thermoplastic nanochannels  
14 following this fabrication scheme were sensitive to: (i) Surface uniformity of the sputtered Al  
15 film; (ii) the extent of uniformity of the silane layer vapor deposited onto the Si master; (iii)  
16 required dosage for complete curing of the UV resin; (iv) the strength of adhesion between the  
17 cured resin stamp and the COC back plate - strong adhesion was achieved by slightly roughening  
18 the COC with a very fine sandpaper, cleaning with water and drying prior to pressing onto the  
19 deposited uncured resin; (v) uniformity of the applied force over the entire substrate area during  
20 thermal embossing; and (vi) the cooling temperature during demolding - a temperature 40 to  
21  $50^\circ\text{C}$  less than the embossing or assembly temperatures was found to yield the most intact and  
22 uniform nanofluidic structures after demolding. Sub-30 nm channels were sensitive to any minor  
23 variation in these parameters as evidenced by small differences in the channel width measured  
24 along the 20 nm deep nanochannel (Figure 1k).  
25  
26  
27  
28  
29  
30  
31  
32  
33  
34  
35  
36  
37  
38  
39  
40  
41  
42  
43  
44  
45  
46  
47

48 Compared to using the patterned Si directly as the embossing stamp, the UV resin stamp  
49 possesses a lower Young's modulus ( $600\text{-}800 \text{ MPa}$ )<sup>56</sup> and a thermal expansion coefficient that is  
50 similar to that of PMMA ( $6 \times 10^{-5}/^\circ\text{C}$ ). This leads to a reduction in the adhesion and thermal  
51 stress during thermal embossing of the nanofluidic device<sup>57,58</sup> producing nanofluidic devices  
52  
53  
54  
55  
56  
57  
58  
59  
60

1  
2  
3 with high structural integrity. A single 4 inch Si wafer could contain 10 - 15 patterned devices  
4  
5 with each Si master used repeatedly to fabricate > 20 UV resin stamps. Each resin stamp could  
6  
7 be then be used for the embossing of >20 replicas in PMMA without noticeable damage.  
8  
9

10 PMMA substrates were sealed using plasma-assisted low temperature thermal fusion bonding  
11 (Figure 2a). The formation of leak-free fluidic devices or discontinuities due to channel collapse  
12 during assembly was evaluated by introducing 5 mM fluorescein in 0.5X TBE buffer into the  
13 fluidic network. As shown in Figures 2b and 2c, the nanoslits and nanochannels did not reveal  
14 any leakage or discontinuity along the channel length. Current-voltage plots acquired after filling  
15 with 1 mM KCl (Figure 2d) revealed that the measured currents for voltages of opposite polarity  
16 had similar absolute values and good linearity (non-rectification). The absence of voltage gating  
17 and rectification indicated homogeneity in surface charge along the walls of the PMMA nanoslits  
18 and nanochannels when using symmetrical electrolyte conditions. Using low thermal bonding  
19 temperatures (~80°C) also minimized the amount of surface reorganization of the polar  
20 functional groups following plasma treatment (Figure S2).  
21  
22  
23  
24  
25  
26  
27  
28  
29  
30  
31  
32  
33  
34  
35

36  
37 **PMMA surface modification.** The surface wettability and solid surface tensions for the  
38 unmodified (u), plasma (O<sub>2</sub>) and amine (NH<sub>2</sub>)-modified PMMA were assessed using water  
39 contact angle measurements (see SI). u-PMMA showed a contact angle of 71.4 ±1.5°, which  
40 corresponded to a solid-vapor surface tension,  $\gamma_{sv}$ , of ~40.4 mJ/m<sup>2</sup>. After plasma treatment, the  
41 contact angle decreased to 50.1 ±1.1° indicating an increase in  $\gamma_{sv}$  to ~54.6 mJ/m<sup>2</sup>. Amine  
42 modification led to an increase in the water contact angle to 62.9 ±2.0° ( $\gamma_{sv} = 45.8$  mJ/m<sup>2</sup>). The  
43 observed trends were consistent with literature data.<sup>40</sup>  
44  
45  
46  
47  
48  
49  
50  
51  
52

53 We also employed XPS and FTIR to analyze the u-PMMA, O<sub>2</sub>-PMMA and NH<sub>2</sub>-PMMA  
54 surfaces to verify the fidelity of the surface modification. The O/C and N/C ratios were used to  
55  
56  
57  
58  
59  
60

1  
2  
3 assess the extent of surface modification of PMMA surfaces (see SI and Figure S4 for summary  
4 of the results). Furthermore, FTIR was employed to characterize the functional groups present on  
5  
6 u-, O<sub>2</sub>- and NH<sub>2</sub>-PMMA surfaces. This data is summarized in the SI and Figure S5. The XPS and  
7  
8 FTIR data confirmed the success of the surface modifications.  
9  
10

11  
12 **Surface topographical studies of modified PMMA nanoslits.** Surface modification reactions  
13 induce not only chemical changes but also some topographical changes. These changes are in the  
14 form of nanometer or sub-nanometer random surface roughness on solid walls with roughness  
15 amplitude  $a_r$ . Results obtained from previously reported molecular dynamic simulations showed  
16 that roughness may affect the wettability of surfaces and the EOF in nanofluidic channels  
17 depends on the magnitude of  $a_r$ .<sup>59</sup> For cases where  $\lambda_D/a_r \ll 1$ , where  $\lambda_D$  is the Debye length, the  
18 EOF can be significantly different compared to  $\lambda_D/a_r \sim 1$ ; the presence of a rough surface that is  
19 comparable to  $\lambda_D$  can alter the EDL near the surface and reduce the EOF<sup>60</sup> and streaming  
20 potential.<sup>61</sup> For a homogeneously charged rough channel surface, the EOF is expected to  
21 decrease when  $a_r$  is >5% of the channel width irrespective of the value of  $\lambda_D/a_r$ .<sup>62</sup> Alterations in  
22 the EOF become insignificant for surfaces with  $\lambda_D/a_r > 1$ .<sup>63,59</sup> Also, the water contact angle is  
23 expected to be altered by rough surfaces compared to a smooth surface with identical chemical  
24 properties.<sup>64,65</sup>  
25  
26  
27  
28  
29  
30  
31  
32  
33  
34  
35  
36  
37  
38  
39  
40  
41  
42

43 The roughness was measured by AFM for PMMA nanoslits because the bottom surface  
44 could be easily profiled without tip-wall interactions compared to nanochannels. Figure 3a shows  
45 a representative AFM image of a nanoslit. For the u-PMMA nanoslit shown in Figure 3b, the  
46 measured RMS surface roughness was 0.75 nm. This value was approximately equal to the  
47 measured roughness obtained from the bottom surface of the FIB milled nanoslit in the original  
48 Si master (data not shown). However, this value was less than that of the planar u-PMMA (1.16  
49  
50  
51  
52  
53  
54  
55  
56  
57  
58  
59  
60

1  
2  
3 nm, see Figure 3e). After surface activation and modification, there was an increase in the RMS  
4  
5 roughness to 0.96 nm and 1.08 nm for the O<sub>2</sub>- and NH<sub>2</sub>-PMMA nanoslits, respectively (Figures  
6  
7 3c and d). This increase in surface roughness for O<sub>2</sub>-PMMA was due to etching by the oxygen  
8  
9 plasma while the surface roughness for the aminated surface can be attributed to slight swelling  
10  
11 and/or dissolution of the PMMA by the EDA solution and the additional C-C bonds introduced  
12  
13 onto the surface from EDA. An increase in the surface roughness was also observed on the  
14  
15 planar O<sub>2</sub>-PMMA and the NH<sub>2</sub>-PMMA compared to u-PMMA (see Figures 3f-g). Nevertheless,  
16  
17 because the experiments were performed at solution ionic strengths where  $\lambda_D < 10 \times$  the channel  
18  
19 dimension but slightly larger than the wall roughness ( $\lambda_D \sim 1.5$  nm),<sup>17,66</sup> we expect the  
20  
21 contributions of surface roughness to wettability and EOF in our PMMA nanoslit and  
22  
23 nanochannel devices to be insignificant relative to contributions from changes in surface charge.  
24  
25  
26  
27  
28

29 **Surface charge and pH effects.** As shown in Figure S6, the nanofluidic device was comprised  
30  
31 of input/output microchannels interconnected by an array of nanochannels with the majority of  
32  
33 the voltage drop occurring across the nanochannels (see Table S1 for resistance values of the  
34  
35 fluidic network). Therefore, the majority of the electrokinetic flow occurred within the  
36  
37 nanochannels, which can be heavily influenced by surface charge and  $\lambda_D$  to name a few. The  
38  
39 surface charge can be a significant determinant of the fluid dynamics for devices possessing high  
40  
41 surface-to-volume ratios. Depending on the solution pH and the surface chemistry, the solid can  
42  
43 have either a positive or negative surface charge density,  $\sigma_s$ , described by  $\sigma_s = \sum_i q_i / A$ ; where  $q_i =$   
44  
45  $z_i e$  and  $q_i$  is the net charge of ion  $i$ ,  $z_i$  is the valency of ion  $i$ ,  $e$  is the electron charge, and  $A$  is the  
46  
47 surface area; this can be used to compute the number of charged sites per unit area,  $\Gamma$  in nm<sup>-2</sup>.<sup>66</sup>  
48  
49  
50  
51 Due to wall surface charge, an EDL develops to maintain the electroneutrality at the solid/liquid  
52  
53  
54  
55  
56  
57  
58  
59  
60

interface.<sup>67</sup> For a channel filled with a symmetrical 1:1 electrolyte such as KCl with ionic concentration  $c$ , the EDL thickness or  $\lambda_D$  is;

$$\lambda_D = \left( \frac{\epsilon_0 \epsilon_r R T}{2 F^2 c} \right)^{1/2} \quad (1)$$

where  $R$  is the gas constant ( $\text{J}\cdot\text{mol}^{-1}\text{K}^{-1}$ ),  $\epsilon_0$  is the permittivity of vacuum ( $\text{F}\cdot\text{m}^{-1}$ ),  $\epsilon_r$  is the dielectric constant of the medium,  $F$  is the Faraday constant ( $\text{C}\cdot\text{m}^{-1}$ ), and  $T$  is the temperature (K).  $\lambda_D$  can vary from  $<1$  nm at high ionic strength to a few tens of nm at low ionic strength.<sup>27</sup>

Electrical conductance measurements across nanofluidic channels filled with ionic salt solutions have been used to deduce the magnitude of the surface charge density. Here, we present a modified electrokinetic model based on the report from Stein *et al.*<sup>28</sup> for determining  $\sigma_s$ . When an external electric field is applied across a nanochannel filled with an ionic salt solution, the measured electrical conductance ( $G_T$ ) is the sum of the bulk conductance ( $G_B$ ) and the surface conductance ( $G_S$ ). At high salt concentrations, the surface charges in the nanochannel are shielded by the mobile ions and have negligible influence on the ion concentration in the nanochannel. In this case, transport is dominated by the ions in the bulk solution and  $G_B$  depends on the nanochannel dimensions and electrolyte concentration according to;<sup>55,66,46</sup>

$$G_B = 10^3 \left( \mu_{\text{K}^+} + \mu_{\text{Cl}^-} \right) c N_A e \cdot \frac{n w h}{L} \quad (2)$$

where  $w$ ,  $L$  and  $h$  are the nanochannel width, length and height, respectively,  $N_A$  is Avogadro's number,  $c$  is the electrolyte concentration in mol/L,  $n$  is the number of nanochannels in the device and  $\mu_{\text{K}^+}$  and  $\mu_{\text{Cl}^-}$  are the ion mobilities of  $\text{K}^+$  and  $\text{Cl}^-$  ions, respectively ( $\mu_{\text{K}^+} = 7.619 \times 10^{-8} \text{ m}^2/\text{V s}$  and  $\mu_{\text{Cl}^-} = 7.912 \times 10^{-8} \text{ m}^2/\text{V s}$ ). However, at low salt concentrations, the nanochannels become predominantly filled with counterions. For electroneutrality within the nanochannel, excess counterions in the EDL compensate for the net surface charge, which governs the counterion concentration inside the channel (see equation S9 in SI).<sup>68</sup>  $G_B$  becomes negligible and

$\sigma_s$  governs the total ion conductance in the nanochannel. For 1D nanoslits such as reported by Stein *et al.*,<sup>28</sup> Schoch *et al.*,<sup>55</sup> Karnik *et al.*,<sup>29</sup> and Martins *et al.*,<sup>46</sup>  $h \ll w$ ; hence  $(w + h) \approx w$ . However, for 2D nanochannels with  $h \leq w$ , the channel width also contributes to  $G_S$ ;

$$G_S = 2 \mu_{opp} \sigma_s n \frac{(w + h)}{L} \quad (3)$$

Hence, the measured electrical conductance is represented as;

$$G_T = 10^3 \left( \mu_{K^+} + \mu_{Cl^-} \right) c N_A e \cdot \frac{n w h}{L} + 2 \mu_{opp} \sigma_s n \frac{(w + h)}{L} \quad (4)$$

(Complete derivation of equation (4) is shown in the SI). When  $G_B \approx G_S$ , a transition ion concentration,  $c_t$ , is observed on a log-log plot of  $G_T$  versus the ion concentration.<sup>55</sup>

We investigated the effects of surface modification of polymer nanofluidic devices by experimentally measuring  $\sigma_s$  of modified PMMA nanoslits and nanochannels by monitoring ionic conductance plots. Figures 4a and 4b show the conductance traces for an array of surface modified nanoslits ( $22 \mu\text{m} \times 1 \mu\text{m} \times 50 \text{nm}$ ) and nanochannels ( $45 \mu\text{m} \times 120 \text{nm} \times 120 \text{nm}$ ) measured over a range of KCl concentrations ( $10^{-5} \text{M} - 1 \text{M}$  in Tris buffer, pH = 7.8). In both devices, the conductance results obtained before and after surface modification differed essentially in the low ionic concentration regime. This effect was characterized by a shift of the plateau conductance suggesting a change in the surface charge dependent on the nature of the modification. When the modified surfaces were in contact with an electrolyte at pH 7.8, ~99.9% of the surface carboxyl groups ( $\text{pK}_a = 4.66$ ) would be deprotonated and ~99.0% of the amine groups ( $\text{pK}_a = 10.42$ ) would be protonated.<sup>69</sup> At extreme pH values and low buffer concentrations, the counterions in solution necessary to maintain electroneutrality are  $\text{H}^+$  and  $\text{K}^+$  for  $\text{O}_2$ -PMMA devices and  $\text{Cl}^-$  and  $\text{OH}^-$  for the  $\text{NH}_2$ -PMMA devices. However, at pH 7.8 and KCl concentration  $\geq 10^{-5} \text{M}$ ,  $[\text{K}^+] \gg [\text{H}^+]$  and  $[\text{Cl}^-] \gg [\text{OH}^-]$ . Therefore in equation (4) (and

equation (S11)),  $\mu_{opp} \approx \mu_{K^+}$  or  $\mu_{Cl^-}$  for the deprotonated and protonated carboxyl and amine surfaces, respectively.<sup>70</sup>

At a KCl concentration greater than  $10^{-2}$  M, the measured ionic conductance in both the nanoslits and nanochannels fit linearly to the theoretical bulk conductance (Figure 4) and was reproducible from one device to another. This confirmed that there was no significant change in the dimensions of the fluidic channels during thermal embossing, device assembly and surface chemical modification. However, at low electrolyte concentrations (surface charge-governed regime), the nanochannel conductance deviated from linearity and plateaued for both the plasma and amine treated devices with the measured surface conductance lower for the  $-NH_3^+$  terminated devices compared to the  $-COO^-$  terminated devices. For the nanoslit devices, the average surface conductance at this region was  $7.5 \times 10^{-10}$  S for the  $O_2$ -PMMA device. After amination, the conductance dropped to  $3.8 \times 10^{-10}$  S,  $\sim 50.7\%$  of its original value (Figure 4A). The transition concentration,  $c_t$ , used to compute  $\sigma_s$  was approximately 6.60 mM and 3.52 mM for the  $O_2$ - and  $NH_2$ -PMMA surfaces, respectively. For  $O_2$ -PMMA nanoslits, we obtained  $|\sigma_s| \sim 38.2$  mC/m<sup>2</sup>, which was less than 60 mC/m<sup>2</sup> reported by Stein *et al.*<sup>28</sup> and 214 mC/m<sup>2</sup> reported by Schoch *et al.*<sup>55</sup> for glass-based nanoslits measured at pH 8. For the  $NH_2$ -PMMA nanoslit,  $|\sigma_s|$  was 28.4 mC/m<sup>2</sup>. In the nanochannels, the conductance in the low ionic strength region for the amine-modified device dropped to  $\sim 67.6\%$  of its  $O_2$ -PMMA device. The surface charge densities were 40.5 mC/m<sup>2</sup> and 22.9 mC/m<sup>2</sup> for the  $O_2$ - and  $NH_2$ -PMMA devices, respectively.

We also monitored the effect of pH on  $\sigma_s$  of PMMA nanoslits and nanochannels. As depicted in Figure 5, the plasma modified nanoslits and nanochannels indicated that the surface charge density gradually increased as the pH of the electrolyte solution increased because at low pH the surface carboxyl groups were converted to their protonated form. This leads to a corresponding

1  
2  
3 decrease in the surface conductance as less counterions are attracted into the fluidic channel. At  
4  
5 high pH, the carboxyl groups become deprotonated thereby increasing  $\sigma_s$ . An opposite trend was  
6  
7 observed for the amine modified surfaces. The measured surface conductance was higher at low  
8  
9 pH and lower at high pH. This is most likely due to the conversion of the  $-\text{NH}_2$  groups to  $-\text{NH}_3^+$   
10  
11 groups at low pH. At  $\text{pH} \geq 8$ , the surfaces of the  $\text{O}_2$ -PMMA devices were fully deprotonated and  
12  
13 the  $|\sigma_s|$  for the nanochannel was found to be greater than the nanoslits. The values were  $38.3$   
14  
15  $\text{mC}/\text{m}^2$  ( $\Gamma \approx 4.2 \text{ nm}^{-2}$ ) and  $40.5 \text{ mC}/\text{m}^2$  ( $\Gamma \approx 4.0 \text{ nm}^{-2}$ ) for the fully deprotonated PMMA nanoslit  
16  
17 and nanochannel, respectively. These values were found to remain relatively constant at  $\text{pH} > 10$ .  
18  
19 In the nanochannel, the width is comparable to the height, therefore, the surface charge density  
20  
21 of the vertical walls, which is typically neglected in the nanoslit, also contributes to the ion  
22  
23 transport within the channel.<sup>71</sup> Surplus counterions would be attracted into the nanochannel and  
24  
25 more coions would be excluded.

26  
27  
28  
29  
30  
31  
32 **EOF measurements.** The EOF can be described in terms of a mobility,  $\mu_{eof} = \mathbf{v}_{eof}/E$ , where  $\mathbf{v}_{eof}$   
33  
34 is the steady-state bulk EOF. At low  $\lambda_D$ ,  $\mu_{eof}$  can be represented in terms of the bulk solvent  
35  
36 viscosity  $\eta_o$ , and the zeta potential  $\zeta$  by the Helmholtz-Smoluchowski relation:<sup>72</sup>  
37

$$\mu_{eof} = \frac{\epsilon_0 \epsilon_r \zeta}{\eta_o} \quad (5)$$

38  
39  
40  
41  
42 Also, the zeta potential can be represented in terms of  $\sigma_s$  and  $\lambda_D$  for different electrolyte solutions  
43  
44 by combining equations (9) into (10):<sup>42</sup>  
45

$$\zeta = \frac{2 k_B T}{e} \ln \left[ \frac{2 e \sigma_s \lambda_D}{\epsilon_r \epsilon_0 k_B T} + \sqrt{1 + \left[ \frac{(e \lambda_D / \epsilon_r \epsilon_0 k_B T)^2}{4} \right]} \right] \quad (6)$$

46  
47  
48  
49  
50  
51  
52 With  $\epsilon_0$  and  $\epsilon_r$  constants, conditions that change  $\sigma_s$ ,  $\zeta$ ,  $\lambda_D$ , or  $\eta$  will alter the magnitude of the  
53  
54 EOF.  $\mu_{eof}$  was measured using the current monitoring method.<sup>73</sup> For the EOF measurement, we  
55  
56 used PMMA devices possessing a single nanofluidic channel  $138 \mu\text{m}$  long and  $0.1 \text{ M}$  and  $0.05 \text{ M}$   
57  
58  
59  
60

1  
2  
3 KCl solutions to allow for the generation of a large amount of readable current (see Figure S6c  
4 for a typical current trace) and to ensure that the measurement was performed at a region where  
5  
6 equation (5) is valid ( $\lambda_D \leq 2$  nm). This single channel geometry eliminates errors in migration  
7  
8 time that may arise due to preferential filling across an array of nanochannels during electrolyte  
9  
10 replacement. A negative EOF value indicated that the EOF was from cathode to anode and  
11  
12 consistent with a positively charged fluidic channel wall while a positive EOF value indicated a  
13  
14 negatively charged wall. Molecular Dynamics (MD) simulations reported by Qiao *et al.*<sup>70</sup> have  
15  
16 revealed that differences in the distribution of counterions for negatively charged O<sub>2</sub>-PMMA  
17  
18 devices when compared to the positively charged NH<sub>2</sub>-PMMA is influenced by the finite size of  
19  
20 the ions - K<sup>+</sup> (0.27 nm) and Cl<sup>-</sup> (0.36 nm) and the EOF is influenced by surface fluid interactions.  
21  
22  
23  
24  
25  
26

27 In previous work, we have shown that exposing PMMA microchannels to controlled plasma  
28  
29 conditions can generate carboxylate groups with a surface coverage of  $2.7 \pm 0.5 \times 10^{-9}$   
30  
31 mol/cm<sup>2</sup>.<sup>44</sup> We have also reported the EOF at pH 7.4 for carboxylated and NH<sub>2</sub>-terminated  
32  
33 PMMA microfluidic devices to be  $4.43 \pm 0.58 \times 10^{-4}$  cm<sup>2</sup>/Vs and  $-1.34 \pm 0.21 \times 10^{-4}$  cm<sup>2</sup>/Vs,  
34  
35 respectively.<sup>38</sup> As shown in Table 1, we obtained an EOF of  $0.93 \pm 0.03 \times 10^{-4}$  cm<sup>2</sup>/Vs and  $-0.82$   
36  
37  $\pm 0.01 \times 10^{-4}$  cm<sup>2</sup>/Vs for O<sub>2</sub>- and NH<sub>2</sub>-PMMA nanoslits, respectively. For the O<sub>2</sub>- and NH<sub>2</sub>-  
38  
39 PMMA nanochannels, the EOF was found to be  $1.02 \pm 0.02 \times 10^{-4}$  cm<sup>2</sup>/Vs and  $-0.75 \pm 0.02 \times 10^{-4}$   
40  
41 cm<sup>2</sup>/Vs, respectively. The trend and magnitude of the EOF observed in the PMMA nanofluidic  
42  
43 devices scales with the measured  $\sigma_s$  in the nanochannel and was consistent with molecular  
44  
45 dynamic simulations reported by Qiao *et al.*<sup>74</sup> The values reported for the O<sub>2</sub>-PMMA  
46  
47 nanochannels were similar to that reported by Menard *et al.*<sup>17</sup> for fused silica nanochannels  
48  
49 ( $\leq 100$  nm) measured using 2× TBE with 2% polyvinylpyrrolidone acting as an EOF suppressor  
50  
51 ( $0.79 \pm 0.01 \times 10^{-4}$  cm<sup>2</sup>/Vs) and  $\sim 35.8 \pm 4.4\%$  lower when compared to fused silica channels  
52  
53  
54  
55  
56  
57  
58  
59  
60

1  
2  
3 measured with 2× TBE only ( $1.58 \pm 0.01 \times 10^{-4} \text{ cm}^2/\text{Vs}$ ). A possible reason for the lower EOF  
4  
5 observed in the PMMA nanofluidic devices is the low  $\zeta$ . This conclusion is supported by the  
6  
7 results from the continuum theory based on the Poisson–Boltzmann equation for the ion  
8  
9 distribution, Navier–Stokes equations for fluid transport<sup>72</sup> and atomistic simulations.<sup>74</sup> Both  
10  
11 models showed that the EOF in a nanofluidic channel varies almost linearly with  $\zeta$  with the latter  
12  
13 model true for surface charge densities  $\leq 80 \text{ mC/m}^2$ .<sup>74</sup> Furthermore,  $\zeta$  depends on the chemistry of  
14  
15 the solid–liquid interface and is related to the surface charge density by parameters such as the  
16  
17 ionic strength, density of charged sites on the surface, their  $\text{pK}_a$  values and the solution pH,  
18  
19 which modulates the extent of dissociation of the surface groups (Figure 5).

20  
21  
22 In addition, recent reports have shown that reducing the size of fluidic channels can result in  
23  
24 reductions of the EOF due to the apparent increase in the viscosity of a fluid upon confinement  
25  
26 in charged nanoconduits,<sup>75-78</sup> an effect not considered in equation (5). In most cases, this  
27  
28 phenomenon makes the ratio of the apparent to predicted or bulk viscosity, represented as  $\eta_{app}/\eta_o$ ,  
29  
30 to exceed 1.3 with this ratio dependent on the material of the channel walls, size and shape of the  
31  
32 channel, the ionic concentration,  $\zeta$ , temperature, and dielectric constant.<sup>77</sup> Due to the relatively  
33  
34 higher  $\zeta$  in glass-based devices,  $\eta_{app}/\eta_o$  is expected to be greater when compared to thermoplastic  
35  
36 devices. This may explain why the EOF measured in glass nanoslits at pH 8.5 ( $\sim 1.3 \times 10^{-4}$   
37  
38  $\text{cm}^2/\text{Vs}$ ) was lower than those of fused silica micro-capillaries ( $5 \times 10^{-4} \text{ cm}^2/\text{Vs}$ )<sup>79</sup> or glass  
39  
40 microchannels ( $4.82 \times 10^{-4} \text{ cm}^2/\text{Vs}$ ).<sup>80</sup>

41  
42  
43 **Transport dynamics of  $\lambda$ -DNA through thermoplastic nanochannels.** The majority of  
44  
45 applications explored in nanofluidic devices have focused on investigating the transport  
46  
47 properties of dsDNA confined in fused silica glass<sup>17, 81-86</sup> and elastomeric<sup>87, 88</sup> nanochannels.  
48  
49 However, because thermoplastics possess dissimilar surface properties compared to glass-based  
50  
51  
52  
53  
54  
55  
56  
57  
58  
59  
60

1  
2  
3 devices,<sup>30</sup> it becomes necessary to explore the transport properties of dsDNA in these devices.  
4  
5 Although, a few studies have utilized PMMA-based nanoslits<sup>32</sup> and nanochannels<sup>89, 90</sup> for DNA  
6  
7 stretching, the electrokinetic parameters of dsDNA in surface modified thermoplastic 2D  
8  
9 nanochannels is yet to be reported. Understanding the effects of  $\sigma_s$  and the charge polarity on  
10  
11 these parameters and on the stretching properties of dsDNA in thermoplastic nanochannels is  
12  
13 necessary for assessing the viability of these devices for applications in DNA sizing or mapping.  
14  
15

16  
17 First, we assessed the degree of extension of dsDNA confined in O<sub>2</sub>-PMMA nanochannels  
18  
19 seeded with 2× TBE buffer (pH 7.5). When a DNA molecule with width  $w$  was driven from a  
20  
21 microchannel into the nanochannel under a constant field, upon initial entrance (also called DNA  
22  
23 injection), the molecule was observed to stretch because the pulling electric force acted against  
24  
25 the resistance due to the entropic interface and frictional forces experienced by the portion of the  
26  
27 molecule resident in the microchannel (red trace and insert in Figure 6a).<sup>86</sup> When the field was  
28  
29 turned off after the molecule had fully entered the nanochannel, the molecule underwent elastic  
30  
31 relaxation and attained an equilibrium extension length shorter than the injection length (blue  
32  
33 trace and insert of Figure 6a). Assuming that the nanochannel has a depth  $D$ , which is less than  
34  
35 the free-solution radius of gyration but greater than the persistence length  $l_p$  of the molecule, due  
36  
37 to self-avoidance the confined molecule will extend in such a way that it divides into a series of  
38  
39 non-interpenetrating blobs with the molecular mass distributed along the channel with relatively  
40  
41 uniform density.<sup>83</sup> We estimated the extension factor  $\epsilon$  of the confined DNA molecule possessing  
42  
43 an equilibrium extension length  $L_E$  and a contour length  $L_C$  with the equation;  
44  
45  
46  
47  
48  
49

$$\frac{L_E}{L_C} \approx \frac{(l_p w)^{1/3}}{D^{2/3}} \quad (7)$$

50  
51 Although, the total contour length of an unstained  $\lambda$ -DNA molecule (48.5 kbp) is 16.3  $\mu\text{m}$ , at our  
52  
53 intercalating dye concentration, we expect a 23% increase in length to 20  $\mu\text{m}$ .<sup>82</sup> Therefore, from  
54  
55  
56  
57  
58  
59  
60

1  
2  
3 equation (7), we expect the extension factor for a stained  $\lambda$ -DNA molecule with a width of 3  
4 nm<sup>91</sup> and persistence length of 50 nm confined in a 100 × 100 nm nanochannel to be ~0.25.  
5  
6  
7  
8 Nevertheless, we note that equation (7) does not account for ionic effects, like the buffer ionic  
9 strength and viscosity, on the elasticity and wall wettability, roughness and frictional drag on the  
10 overall extension of the DNA molecule.<sup>81, 92, 93</sup>  
11  
12  
13

14  
15 In our experiment, we observed that when stained  $\lambda$ -DNA molecules were completely  
16 introduced into the O<sub>2</sub>-PMMA nanochannels, it stretched to ~11.25 ± 1.68  $\mu$ m at initial entry  
17 (calculated from  $n = 20$ ). When the field was turned off, the DNA molecules remained confined  
18 in the nanochannel but relaxed to an overall average extension length of 6.88  $\mu$ m, determined  
19 from a Gaussian curve fit of the histogram shown in Figure 6b. The experimental extension  
20 factor was 0.34, a value ~40% greater than that predicted by the de Gennes theory. The enhanced  
21 stretching of the confined DNA molecule was likely due to additional interfacial surface forces  
22 in the form of surface energy acting on the DNA molecule from the charged nanochannel walls.  
23  
24  
25  
26  
27  
28  
29  
30  
31  
32  
33  
34  
35 The measured surface energy for O<sub>2</sub>-PMMA devices was ~38.9 mJ/m<sup>2</sup> (see Figure S3 in SI).

36  
37 Next, we investigated the electrophoretic properties of DNA molecules electrokinetically  
38 driven through nanochannels using 50  $\mu$ m long, 100 nm × 100 nm channels. All DNA  
39 movements represented in the frames shown in Figures 6c and 6d were observed without the  
40 need of an EOF suppressor. The apparent electrophoretic mobility  $\mu_{app}$  of DNA in the  
41 nanochannel was due to the electrophoretic mobility of DNA,  $\mu_{ep}$ , and the EOF.  
42  
43  
44  
45  
46  
47

48  
49 Figure 6e shows the variation of  $\mu_{app}$  for  $\lambda$ -DNA traveling through O<sub>2</sub>-PMMA nanochannels  
50 filled with 0.5× (black squares) and 2× (red circles) TBE. Our results revealed that the apparent  
51 mobility of  $\lambda$ -DNA was lower in the channel filled with 0.5× TBE than that of 2× TBE. One  
52 possible reason for this was that as the ionic strength of the buffer solution in the charged  
53  
54  
55  
56  
57  
58  
59  
60

1  
2  
3  
4  
5  
6  
7  
8  
9  
10  
11  
12  
13  
14  
15  
16  
17  
18  
19  
20  
21  
22  
23  
24  
25  
26  
27  
28  
29  
30  
31  
32  
33  
34  
35  
36  
37  
38  
39  
40  
41  
42  
43  
44  
45  
46  
47  
48  
49  
50  
51  
52  
53  
54  
55  
56  
57  
58  
59  
60

nanochannel was reduced, there was a corresponding increase in  $\lambda_D$  (~30 nm for 0.5× and ~8 nm for 2× TBE, estimated from classical theory).<sup>94, 95</sup> This led to a larger EOF for the lower ionic strength buffer thereby reducing  $\mu_{app}$  of  $\lambda$ -DNA molecules through the nanochannel. We observed that in the devices filled with 2× TBE, the DNA moved through the nanochannel with a constant velocity (Figure 6d) and an almost linear variation of the electrophoretic mobility for the entire range of electric field strengths studied (red trace in Figure 6e). This confirmed the absence of dielectrophoretic trapping sites along the channel wall, which was supported by the low nanochannel wall roughness. Interestingly, in the nanochannels seeded with 0.5× TBE, we observed intermittent (stick-slip) motion of the DNA molecules through the nanochannel similar to previous reports<sup>32, 84</sup> at measurements performed <150 V/cm (Figure 6c). Based on MD simulations<sup>96</sup> and theoretical computations,<sup>97</sup> a highly negatively charged DNA molecule translocating through a nanochannel interacts both electrically (attractive or repulsive forces) and hydrodynamically with the channel wall. Therefore, we attributed the intermittent motion of DNA to latent electrical interactions between the charged DNA molecule and the thick EDL and this presents the possibility that at this field strength, the driving force was less than the interfacial force. This observation is yet to be reported for DNAs translocating through glass nanofluidic devices at this field strength because the threshold field strength required to introduce DNA into nanochannels without the addition of an EOF suppressor was >200 V/cm for 100 nm nanochannels.<sup>17</sup> However, at field strengths greater than 200 V/cm, we did not observe intermittent motion of DNA in these devices with 0.5× TBE. It is possible that at these fields, the driving force overwhelmed the interfacial force causing the DNA to move through the nanochannel with continuous velocity or that the wall interactions occurred so fast they were not detectable at our imaging frame rate.

1  
2  
3 Finally, we performed translocation experiments in a  $\text{NH}_2$ -PMMA device using  $2\times$  TBE (pH  
4 7.4). At this pH, we observed that  $\lambda$ -DNA adsorbed onto the surface of the assess microchannels  
5 and remained immobile even with the application of a large bias voltage. This sticking is  
6 probably due to strong electrostatic interactions between the negatively charged DNA backbone  
7 and the positively charged amine groups. When the solution pH was increased to 10, there were  
8 significant reductions in DNA sticking in the microchannel and several  $\lambda$ -DNA molecules were  
9 observed to move towards the entrance of the nanochannel. However, when the DC voltage was  
10 turned on, the DNA molecules initially attempted to enter the nanochannel but paused at first  
11 entry (Figure S7 in SI). No further movement was observed at higher fields and even with  
12 reversed DC voltages. This is likely due to strong wall interactions with residual  $-\text{NH}_3^+$  groups  
13 or hydrogen bonding between the DNA and the deprotonated  $-\text{NH}_2$  groups overwhelming the  
14 electrokinetic driving force.  
15  
16  
17  
18  
19  
20  
21  
22  
23  
24  
25  
26  
27  
28  
29  
30  
31

## 32 CONCLUSIONS

33  
34 In this work, we report a simple and robust fabrication strategy that can be used to produce  
35 thermoplastic nanofluidic devices with structures below 20 nm. Furthermore, because the  
36 fabrication steps were successfully achieved using simple bench top UV curing and thermal  
37 embossing instruments, the cost of device fabrication was significantly reduced compared to  
38 conventional NIL techniques. We demonstrated the successful modification of thermoplastic  
39 nanoslits and nanochannels using oxygen plasma to produce carboxylic acid moieties that could  
40 be subsequently converted into amino groups by reaction with EDA. For the conditions reported  
41 in this work, the plasma treated polymer nanoslits and nanochannels were observed to possess  
42  $|\sigma_s|$  of  $38.2 \text{ mC/m}^2$  and  $40.5 \text{ mC/m}^2$ , respectively, at pH 7.8. These values were lower than that  
43 reported for their glass-based counterparts. The low surface charge densities in polymer  
44  
45  
46  
47  
48  
49  
50  
51  
52  
53  
54  
55  
56  
57  
58  
59  
60

1  
2  
3 nanofluidic devices helped to minimize artifacts arising from ion exclusion due to concentration  
4 polarization. The ability to generate positively charged moieties in a simple modification scheme  
5  
6 with  $|\sigma_s|$  of 28.4  $mC/m^2$  in the nanoslits and 22.9  $mC/m^2$  in the nanochannels offers a unique  
7  
8 venue for performing nanochannel chromatography by generating the proper stationary phase.  
9  
10

11  
12 The reduced EOF observed in PMMA nanofluidic devices compared to polymer  
13 microchannels and glass nanochannels was likely due to lower surface charge density (and zeta  
14 potential) and apparent increases in fluid viscosity due to nanoconfinement. Generally, lower  
15 EOF values are desirable in applications involving DNA analysis for mapping and sequencing  
16 because it enables the introduction of these biomolecules into the fluidic channels without the  
17 need for EOF suppressors.  
18  
19  
20  
21  
22  
23  
24  
25  
26

## 27 28 **ACKNOWLEDGMENTS**

29  
30 The authors would like to thank National Institute of Health (NIH R21HG006278) and the  
31 National Science Foundation (CBET-1067583) for supporting this work. We also acknowledge  
32 Dr. C. Donley of the UNC Chapel Hill Analytical and Nanofabrication Laboratory for assistance  
33 with the XPS data, Dr. A. S. Kumbhar for acquiring the AFM, UNIST Central Research Facility  
34 (UCRF) South Korea for assistance with ATR-FTIR, Dr H. Wang for helpful discussions and the  
35 UNC-Olympus Imaging Research Center.  
36  
37  
38  
39  
40  
41  
42  
43  
44

45 **Supporting Information Available:** Surface energy determinations; XPS/FTIR characterization  
46 of modified PMMA surfaces; electrical model of nanofluidic device; conductance determinations  
47 in nanochannels; DNA translocation through EDA-modified PMMA nanochannels. This material  
48 is available free of charge via the Internet at <http://pubs.rsc.org>.  
49  
50  
51  
52  
53  
54  
55  
56  
57  
58  
59  
60

## REFERENCES

1. J. W. van Honschoten, N. Brunets and N. R. Tas, *Chem. Soc. Rev.*, 2010, **39**, 1096-1114.
2. R. K. Anand, E. Sheridan, K. N. Knust and R. M. Crooks, *Anal. Chem.*, 2011, **83**, 2351-2358.
3. A. Mani, T. A. Zangle and J. G. Santiago, *Langmuir*, 2009, **25**, 3898-3908.
4. Y.-C. Wang, A. L. Stevens and J. Han, *Anal. Chem.*, 2005, **77**, 4293-4299.
5. S. J. Kim, Y.-C. Wang, J. H. Lee, H. Jang and J. Han, *Phys. Rev. Lett.*, 2007, **99**, 044501.
6. S. J. Kim, L. D. Li and J. Han, *Langmuir*, 2009, **25**, 7759-7765.
7. Q. Pu, J. Yun, H. Temkin and S. Liu, *Nano Lett.*, 2004, **4**, 1099-1103.
8. H. Craighead, *Nature*, 2006, **442**, 387-393.
9. H. G. Craighead, *J. Vac. Sci. Technol., A*, 2003, **21**, S216-S221.
10. O. A. Saleh and L. L. Sohn, *Nano Lett.*, 2003, **3**, 37-38.
11. L. D. Menard, C. E. Mair, M. E. Woodson, J. P. Alarie and J. M. Ramsey, *ACS Nano*, 2012, **6**, 9087-9094.
12. T. A. Zangle, A. Mani and J. G. Santiago, *Chem. Soc. Rev.*, 2010, **39**, 1014-1035.
13. A. Piruska, M. Gong, J. V. Sweedler and P. W. Bohn, *Chem. Soc. Rev.*, 2010, **39**, 1060-1072.
14. T. Tsukahara, K. Mawatari and T. Kitamori, *Chem. Soc. Rev.*, 2010, **39**, 1000-1013.
15. U. F. Keyser, S. van Dorp and S. G. Lemay, *Chem. Soc. Rev.*, 2010, **39**, 939-947.
16. S. Pennathur, F. Baldessari, J. G. Santiago, M. G. Kattah, J. B. Steinman and P. J. Utz, *Anal. Chem.*, 2007, **79**, 8316-8322.
17. L. D. Menard and J. M. Ramsey, *Anal. Chem.*, 2013, **85**, 1146-1153.
18. S. J. Kim, S. H. Ko, K. H. Kang and J. Han, *Nat. Nanotechnol.*, 2013, **8**, 609-609.
19. L.-J. Cheng and L. J. Guo, *Chem. Soc. Rev.*, 2010, **39**, 923-938.
20. F. Persson and J. O. Tegenfeldt, *Chem. Soc. Rev.*, 2010, **39**, 985-999.
21. S. L. Levy and H. G. Craighead, *Chem. Soc. Rev.*, 2010, **39**, 1133-1152.
22. X. Liang and S. Y. Chou, *Nano Lett.*, 2008, **8**, 1472-1476.

23. C. H. Reccius, J. T. Mannion, J. D. Cross and H. G. Craighead, *Phys. Rev. Lett.*, 2005, **95**, 268101.
24. S. L. Levy, J. T. Mannion, J. Cheng, C. H. Reccius and H. G. Craighead, *Nano Lett.*, 2008, **8**, 3839-3844.
25. H. Daiguji, *Chem. Soc. Rev.*, 2010, **39**, 901-911.
26. J. Han and H. G. Craighead, *Science*, 2000, **288**, 1026-1029.
27. A. Plecis, R. B. Schoch and P. Renaud, *Nano Lett.*, 2005, **5**, 1147-1155.
28. D. Stein, M. Kruithof and C. Dekker, *Phys. Rev. Lett.*, 2004, **93**, 035901.
29. R. Karnik, K. Castelino, R. Fan, P. Yang and A. Majumdar, *Nano Lett.*, 2005, **5**, 1638-1642.
30. R. Chantiwas, S. Park, S. A. Soper, B. C. Kim, S. Takayama, V. Sunkara, H. Hwang and Y.-K. Cho, *Chem. Soc. Rev.*, 2011, **40**, 3677-3702.
31. S. Y. Chou, P. R. Krauss and P. J. Renstrom, *Appl. Phys. Lett.*, 1995, **67**, 3114-3116.
32. R. Chantiwas, M. L. Hupert, S. R. Pullagurla, S. Balamurugan, J. Tamarit-Lopez, S. Park, P. Datta, J. Goettert, Y.-K. Cho and S. A. Soper, *Lab Chip*, 2010, **10**, 3255-3264.
33. J. Wu, R. Chantiwas, A. Amirsadeghi, S. A. Soper and S. Park, *Lab Chip*, 2011, **11**, 2984-2989.
34. P. Abgrall, L.-N. Low and N.-T. Nguyen, *Lab Chip*, 2007, **7**, 520-522.
35. O. Rotting, W. Ropke, H. Becker and C. Gartner, *Microsyst. Technol.*, 2002, **8**, 32-36.
36. S. A. Soper, A. C. Henry, B. Vaidya, M. Galloway, M. Wabuyele and R. L. McCarley, *Analytica Chimica Acta*, 2002, **470**, 87-99.
37. S. B. Hawthorne, Y. Yang, C. B. Grabanski, D. J. Miller and M. L. Lee, *Anal. Chem.*, 2000, **72**, 642-643.
38. S. L. Llopis, J. Osiri and S. A. Soper, *Electrophoresis*, 2007, **28**, 984-993.
39. J. M. Jackson, M. A. Witek, M. L. Hupert, C. Brady, S. Pullagurla, J. Kamande, R. D. Aufforth, C. J. Tignanelli, R. J. Torphy, J. J. Yeh and S. A. Soper, *Lab Chip*, 2014, **14**, 106-117.
40. A. C. Henry, T. J. Tutt, M. Galloway, Y. Y. Davidson, C. S. McWhorter, S. A. Soper and R. L. McCarley, *Anal. Chem.*, 2000, **72**, 5331-5337.
41. C. M. Chan, T. M. Ko and H. Hiraoka, *Surface Science Reports*, 1996, **24**, 1-54.

- 1  
2  
3  
4  
5  
6  
7  
8  
9  
10  
11  
12  
13  
14  
15  
16  
17  
18  
19  
20  
21  
22  
23  
24  
25  
26  
27  
28  
29  
30  
31  
32  
33  
34  
35  
36  
37  
38  
39  
40  
41  
42  
43  
44  
45  
46  
47  
48  
49  
50  
51  
52  
53  
54  
55  
56  
57  
58  
59  
60
42. J. Chai, F. Lu, B. Li and D. Y. Kwok, *Langmuir*, 2004, **20**, 10919-10927.
  43. S. Wei, B. Vaidya, A. B. Patel, S. A. Soper and R. L. McCarley, *J. Phys. Chem. B*, 2005, **109**, 16988-16996.
  44. F. Xu, P. Datta, H. Wang, S. Gurung, M. Hashimoto, S. Wei, J. Goettert, R. L. McCarley and S. A. Soper, *Anal. Chem.*, 2007, **79**, 9007-9013.
  45. S. C. Yang, *Microfluid. Nanofluid.*, 2006, **2**, 501-511.
  46. D. C. Martins, V. Chu and J. P. Conde, *Biomicrofluidics*, 2013, **7**, 034111 (1-21).
  47. N. R. Tas, J. W. Berenschot, P. Mela, H. V. Jansen, M. Elwenspoek and A. van den Berg, *Nano Lett.*, 2002, **2**, 1031-1032.
  48. L. D. Menard and J. M. Ramsey, *Nano Lett.*, 2011, **11**, 512-517.
  49. D. Huh, K. L. Mills, X. Y. Zhu, M. A. Burns, M. D. Thouless and S. Takayama, *Nat. Mater.*, 2007, **6**, 424-428.
  50. S. Chung, J. H. Lee, M.-W. Moon, J. Han and R. D. Kamm, *Adv. Mater.*, 2008, **20**, 3011-3016.
  51. K. D. Park, S. W. Lee, N. Takama, T. Fujii and B. J. Kim, *Microelectron. Eng.*, 2009, **86**, 1385-1388.
  52. S.-m. Park, Y. S. Huh, H. G. Graighead and D. Erickson, *PNAS*, 2009, **106**, 15549-15554, S15549/15541-S15549/15546.
  53. P. E. Shao, A. van Kan, L. P. Wang, K. Ansari, A. A. Bettioli and F. Watt, *Appl. Phys. Lett.*, 2006, **88**, 093515 (1-3).
  54. R. Kwak, S. J. Kim and J. Han, *Anal. Chem.*, 2011, **83**, 7348-7355.
  55. R. B. Schoch and P. Renaud, *Appl. Phys. Lett.*, 2005, **86**, 25311 25311-25313.
  56. A. Amirsadeghi, J. J. Lee and S. Park, *Appl. Surf. Sci.*, 2011, **258**, 1272-1278.
  57. M. B. Chan-Park, Y. Yan, W. K. Neo, W. Zhou, J. Zhang and C. Y. Yue, *Langmuir*, 2003, **19**, 4371-4380.
  58. H. Becker and C. Gärtner, *Anal. Bioanal. Chem*, 2008, **390**, 89-111.
  59. R. J. Messinger and T. M. Squires, *Phys. Rev. Lett.*, 2010, **105**, 144505 (1-4).
  60. A. S. Ziarani and A. A. Mohamad, *Nanoscale and microscale thermophys. engin.*, 2008, **12**, 154-169.
  61. H. M. Park and H. D. Lee, *Int. J Heat and Mass Transfer*, 2012, **55**, 3295-3306.

- 1  
2  
3  
4  
5  
6  
7  
8  
9  
10  
11  
12  
13  
14  
15  
16  
17  
18  
19  
20  
21  
22  
23  
24  
25  
26  
27  
28  
29  
30  
31  
32  
33  
34  
35  
36  
37  
38  
39  
40  
41  
42  
43  
44  
45  
46  
47  
48  
49  
50  
51  
52  
53  
54  
55  
56  
57  
58  
59  
60
62. M. Wang, J. Wang and S. Chen, *J. Comp. Physics*, 2007, **226**, 836-851.
63. D. Kim and E. Darve, *Phys. Rev. E*, 2006, **73**, 051203.
64. R. N. Wenzel, *J. Phys. and Colloid Chem.*, 1949, **53**, 1466-1467.
65. D. Y. Kwok and A. W. Neumann, *Adv. in Colloid and Interf. Sci.*, 1999, **81**, 167-249.
66. R. B. Schoch, J. Han and P. Renaud, *Rev. of Modern Physics*, 2008, **80**, 839-883.
67. J. Sonnefeld, A. Göbel and W. Vogelsberger, *Colloid Polym Sci*, 1995, **273**, 926-931.
68. H. Daiguji, P. Yang and A. Majumdar, *Nano Lett.*, 2003, **4**, 137-142.
69. G. Meisenberg, *Principles of medical biochemistry*, Mosby Elsevier, Philadelphia, 2006.
70. R. Qiao and N. R. Aluru, *Colloids and Surfaces A: Physicochemical and Engineering Aspects*, 2005, **267**, 103-109.
71. S. Bhattacharyya, Z. Zheng and A. Conlisk, *J. Fluid Mechanics*, 2005, **540**, 247-268.
72. G. Slater, F. Tessier and K. Kopecka, in *Microengineering in Biotechnology*, eds. M. P. Hughes and K. F. Hoettges, Humana Press, 2010, vol. 583, ch. 5, pp. 121-134.
73. X. Huang, M. J. Gordon and R. N. Zare, *Anal. Chem.*, 1988, **60**, 1837-1838.
74. R. Qiao and N. R. Aluru, *Langmuir*, 2005, **21**, 8972-8977.
75. N. R. Tas, J. Haneveld, H. V. Jansen, M. Elwenspoek and A. van den Berg, *Appl. Phys. Lett.*, 2004, **85**, 3274-3276.
76. N. Kaji, R. Ogawa, A. Oki, Y. Horiike, M. Tokeshi and Y. Baba, *Anal. Bioanal. Chem.*, 2006, **386**, 759-764.
77. M. Wang, C.-C. Chang and R.-J. Yang, *J. Chem. Phys.*, 2010, **132**, 024701(1-6).
78. P. Neogi and E. Ruckenstein, *J. Colloid and Interf. Sci.*, 1981, **79**, 159-169.
79. T. Hug, N. d. Rooij and U. Staufer, *Microfluid. Nanofluid.*, 2006, **2**, 117-124.
80. D. Milanova, R. D. Chambers, S. S. Bahga and J. G. Santiago, *Electrophoresis*, 2012, **33**, 3259-3262.
81. J. O. Tegenfeldt, C. Prinz, H. Cao, S. Chou, W. W. Reisner, R. Riehn, Y. M. Wang, E. C. Cox, J. C. Sturm, P. Silberzan and R. H. Austin, *PNAS*, 2004, **101**, 10979-10983.
82. J. T. Mannion, C. H. Reccius, J. D. Cross and H. G. Craighead, *Biophys. J.*, 2006, **90**, 4538-4545.

- 1  
2  
3 83. B. Chu, *JACS*, 1983, **105**, 5169-5169.  
4  
5  
6 84. L. C. Campbell, M. J. Wilkinson, A. Manz, P. Camilleri and C. J. Humphreys, *Lab Chip*,  
7 2004, **4**, 225-229.  
8  
9 85. O. B. Bakajin, T. A. J. Duke, C. F. Chou, S. S. Chan, R. H. Austin and E. C. Cox, *Phys.*  
10 *Rev. Lett.*, 1998, **80**, 2737-2740.  
11  
12 86. C. H. Reccius, S. M. Stavis, J. T. Mannion, L. P. Walker and H. G. Craighead, *Biophys. J.*,  
13 2008, **95**, 273-286.  
14  
15  
16 87. T. Matsuoka, B. C. Kim, J. Huang, N. J. Douville, M. D. Thouless and S. Takayama, *Nano*  
17 *Lett.*, 2012, **12**, 6480-6484.  
18  
19 88. E. Angeli, C. Manneschi, L. Repetto, G. Firpo and U. Valbusa, *Lab Chip*, 2011, **11**, 2625-  
20 2629.  
21  
22  
23 89. H. T. Lasse, K. Anna and K. Anders, *Nanotechnology*, 2008, **19**, 125301.  
24  
25 90. P. Fanzio, V. Mussi, C. Manneschi, E. Angeli, G. Firpo, L. Repetto and U. Valbusa, *Lab*  
26 *Chip*, 2011, **11**, 2961-2966.  
27  
28 91. J. A. Schellman and D. Stigter, *Biopolymers*, 1977, **16**, 1415-1434.  
29  
30 92. W. Reisner, J. P. Beech, N. B. Larsen, H. Flyvbjerg, A. Kristensen and J. O. Tegenfeldt,  
31 *Phys. Rev. Lett.*, 2007, **99**, 058302.  
32  
33 93. C. G. Baumann, S. B. Smith, V. A. Bloomfield and C. Bustamante, *PNAS*, 1997, **94**, 6185-  
34 6190.  
35  
36  
37 94. B. J. Kirby and E. F. Hasselbrink, *Electrophoresis*, 2004, **25**, 187-202.  
38  
39 95. S.-S. Hsieh, H.-C. Lin and C.-Y. Lin, *Colloid Polym Sci*, 2006, **284**, 1275-1286.  
40  
41 96. B. Luan, A. Afzali, S. Harrer, H. Peng, P. Waggoner, S. Polonsky, G. Stolovitzky and G.  
42 Martyna, *J. Phys Chem. B*, 2010, **114**, 17172-17176.  
43  
44  
45 97. L. Binqun and S. Gustavo, *Nanotechnology*, 2013, **24**, 195702.  
46  
47  
48  
49  
50  
51  
52  
53  
54  
55  
56  
57  
58  
59  
60

## Figure Captions

**Figure 1.** Process scheme for the fabrication and assembly of thermoplastic nanofluidic devices. (a) Fabrication of the Si master, which consisted of micron-scale access channels and the nanochannels/nanoslits; (b) fabrication of the protrusive polymer stamp in a UV-curable resin from the Si master; (c) generation of the fluidic structures in the thermoplastic substrate from the resin stamp by thermal embossing and plasma-assisted bonding of the substrate to the cover plate. SEMs of the Si master, resin stamp and PMMA substrate for the nanoslits (d, e, f) and nanochannels (g, h, i), respectively. Inset shows the off-axis ( $52^\circ$ ) cross section SEM images of the Si masters. The dimensions ( $l \times w \times h$ ) were  $22 \mu\text{m} \times 1 \mu\text{m} \times 50 \text{nm}$  for each of the 4 nanoslits and  $45 \mu\text{m} \times 120 \text{nm} \times 120 \text{nm}$  for each of the 7 nanochannels. Series of SEMs for a  $18 \times 23 \text{nm}$  nanochannel in Si (j) and (k) the embossed nanochannel in PMMA. The roughness seen in the SEMs for the stamp and substrate are artifacts from coating with 3 nm AuPd for imaging.

**Figure 2.** (a) Photograph of a thermally assembled nanofluidic devices fabricated in PMMA. The fluorescence images for the sealed nanoslit (b) and nanochannel (c) devices seeded with 5 mM FITC in  $0.5\times$  TBE buffer. (d) I/V plot generated between  $-0.9 \text{V}$  to  $0.9 \text{V}$  for the nanofluidic device filled with 1 mM KCl revealing an electrical conductance of  $90.08 \pm 5.7 \text{nS}$  and  $12.26 \pm 12.3 \text{nS}$  for the nanoslits and nanochannels, respectively. The measured currents have similar absolute values for the respective voltages of opposing polarities; hence, the channels are symmetric (absence of rectification).

**Figure 3.** AFM characterization of a PMMA nanofluidic device with  $1 \mu\text{m} \times 50 \text{nm}$  nanoslit (a) for: (b) u-PMMA; (c)  $\text{O}_2$ -PMMA; and (d)  $\text{NH}_2$ -PMMA. The image shown is  $4 \mu\text{m} \times 500 \text{nm}$ . The measured root-mean-square (RMS) surface roughness was 0.80 nm, 0.95 nm and 1.03 nm, respectively, for these three devices. Also shown are AFM images for planar PMMA; (e) u-PMMA (f)  $\text{O}_2$ -PMMA and (g)  $\text{NH}_2$ -PMMA. Images on the planar PMMA were scanned over an area of  $3.5 \times 3.5 \mu\text{m}$ .

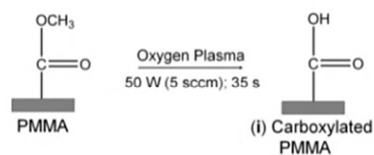
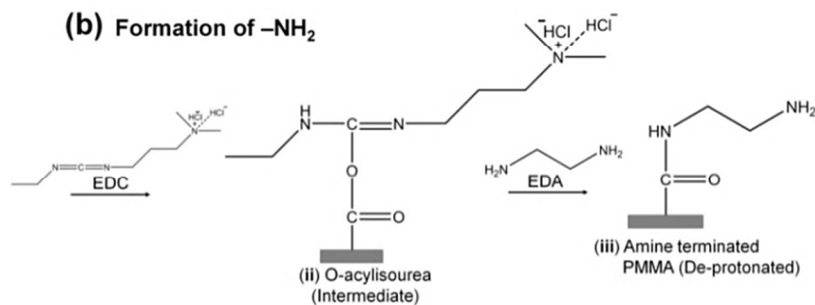
**Figure 4.** Conductance plots obtained from surface modified devices consisting an array of (a) four nanoslits (each  $1 \mu\text{m}$  wide,  $50 \text{nm}$  deep and  $22 \mu\text{m}$  long), and (b) seven nanochannels (each  $120 \text{nm}$  wide,  $120 \text{nm}$  deep and  $45 \mu\text{m}$  long) square and circle markers represent the data obtained for the plasma and amine modified surfaces, respectively. The solid blue line represents the trace of the theoretical bulk conductance calculated with equation (2). Each data point represents an average of five measurements with a scatter in the data within 5-8% of the mean value. From the graph, the effective surface charge density as calculated from the transition concentration,  $c_t$ , was  $38.2 \text{mC/m}^2$  for plasma treated nanoslit,  $28.4 \text{mC/m}^2$  for amine treated nanoslit,  $40.5 \text{mC/m}^2$  for plasma treated nanochannel and  $22.9 \text{mC/m}^2$  for the amine treated nanochannel.

**Figure 5.** Plot showing the effect of pH on the surface charge density  $\sigma_s$ , in plasma and amine modified nanoslits and nanochannels.

**Figure 6.** (a) Representative fluorescence intensity profile of an individual YOYO-1 stained  $\lambda$ -DNA molecule after injection (red line) and confinement (blue line) in the plasma modified nanochannel filled with  $2\times$  TBE buffer. Complete injection into the nanochannel produced an initial molecule length of  $11.25 \pm 1.68 \mu\text{m}$  (calculated from  $n=20$  events). However, when the voltage was turned off, the DNA relaxed to its equilibrium length. (b) Histogram of the measured end-to-end length of relaxed  $\lambda$ -DNA molecules confined in the PMMA nanochannel. The average equilibrium length determined by the Gaussian curve fit (black line) was  $\sim 6.88 \pm 0.43 \mu\text{m}$ .

Representative frames of fluorescently stained  $\lambda$ -DNA molecules translocating through a  $100 \text{nm} \times 100 \text{nm}$  plasma modified PMMA nanochannel and imaged in (c)  $0.5\times$  and (d)  $2\times$  TBE buffer at  $80 \text{V/cm}$  and  $120 \text{V/cm}$ , respectively. The time between frames is approximately 20 ms and scale bars are  $10 \mu\text{m}$ . (e) Plots of DNA apparent mobility against the electric field strength for DNA translocation through the

1  
2  
3 single nanochannel filled with 0.5× (black markers) and 2× (red markers) TBE buffer. Error bars represent  
4 the standard deviations in the measurements (n = 10).  
5  
6  
7  
8  
9  
10  
11  
12  
13  
14  
15  
16  
17  
18  
19  
20  
21  
22  
23  
24  
25  
26  
27  
28  
29  
30  
31  
32  
33  
34  
35  
36  
37  
38  
39  
40  
41  
42  
43  
44  
45  
46  
47  
48  
49  
50  
51  
52  
53  
54  
55  
56  
57  
58  
59  
60

**(a) Formation of -COOH****(b) Formation of -NH<sub>2</sub>**

**Scheme 1.** Protocol for the surface modification of PMMA with (a) carboxyl groups by plasma activation, and (b) amine groups by chemical reaction with ethylenediamine through EDC coupling chemistry to the plasma activated PMMA.

**Table 1.** Measured and expected EOF values as well as surface charge and zeta potentials for the plasma activated and amine terminated devices investigated at pH 7.8.

Device	Terminating groups	$\sigma_s$ (mC/m <sup>2</sup> )	$\zeta$ (mV)	$\mu_{eof}$ (cm <sup>2</sup> /Vs) $\times 10^{-4}$	
				Expected*	Measured
Nanoslit	O <sub>2</sub> -PMMA	- 38.3	- 57.1	4.53	0.93 $\pm$ 0.025
	NH <sub>2</sub> -PMMA	28.4	45.8	- 3.63	- 0.82 $\pm$ 0.012
Nanochannel	O <sub>2</sub> -PMMA	- 40.5	- 59.8	4.74	1.02 $\pm$ 0.017
	NH <sub>2</sub> -PMMA	22.9	38.3	- 3.04	- 0.75 $\pm$ 0.021

\*Calculated from equation (6) using the values for  $\sigma_s$  and  $\zeta$

Figure 1.

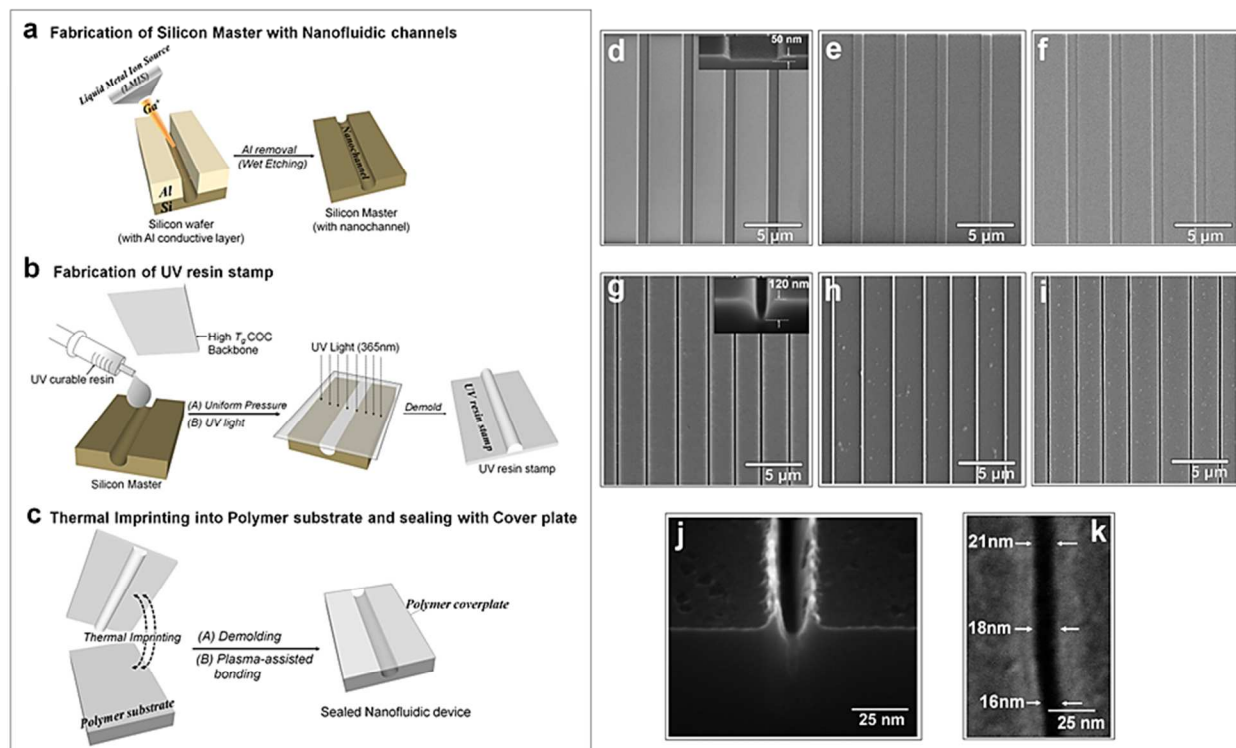


Figure 2.

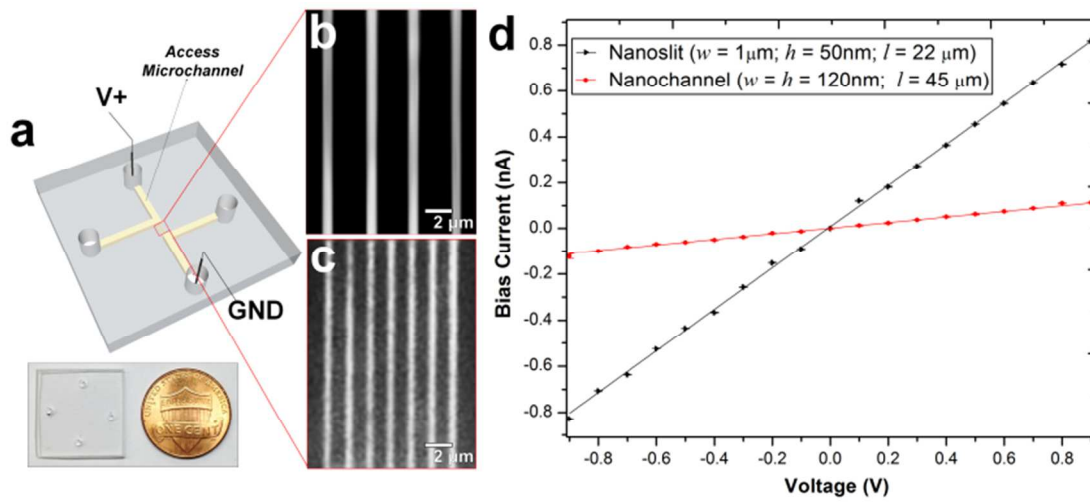


Figure 3.

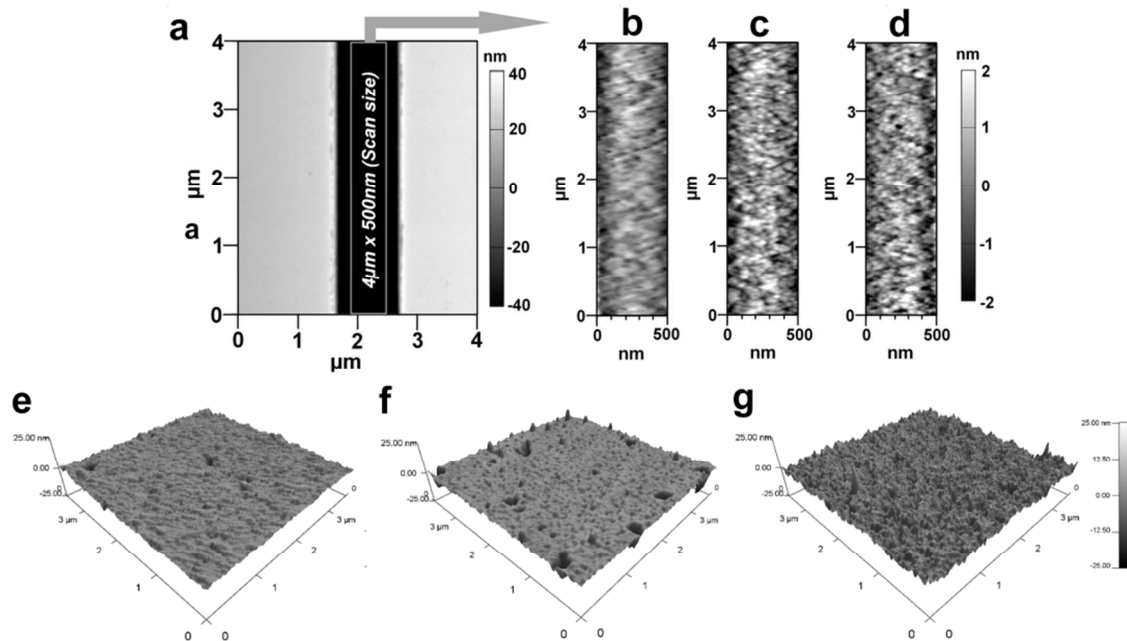


Figure 4.

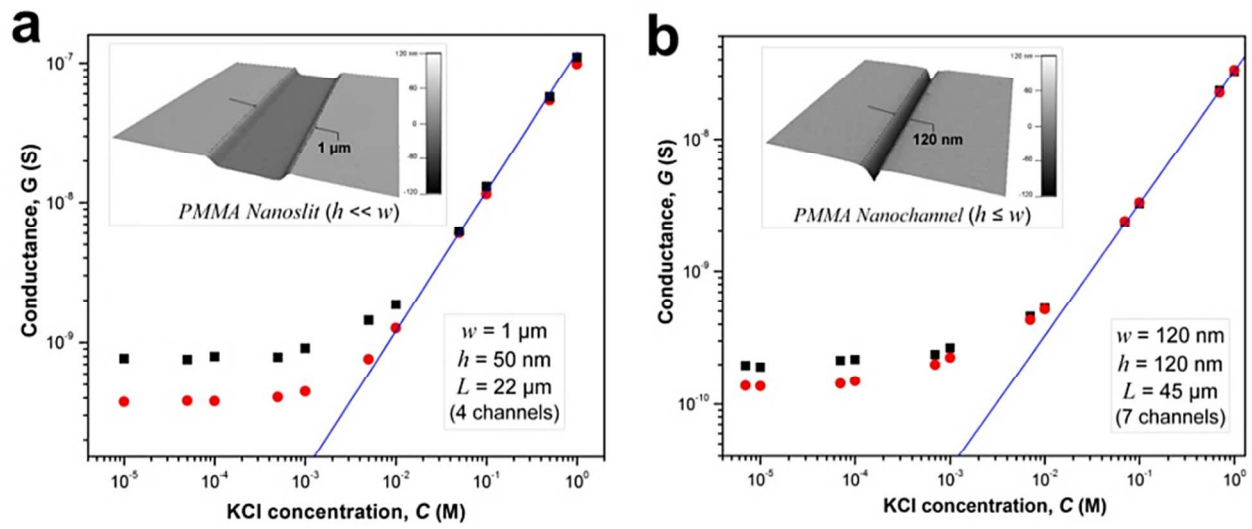


Figure 5.

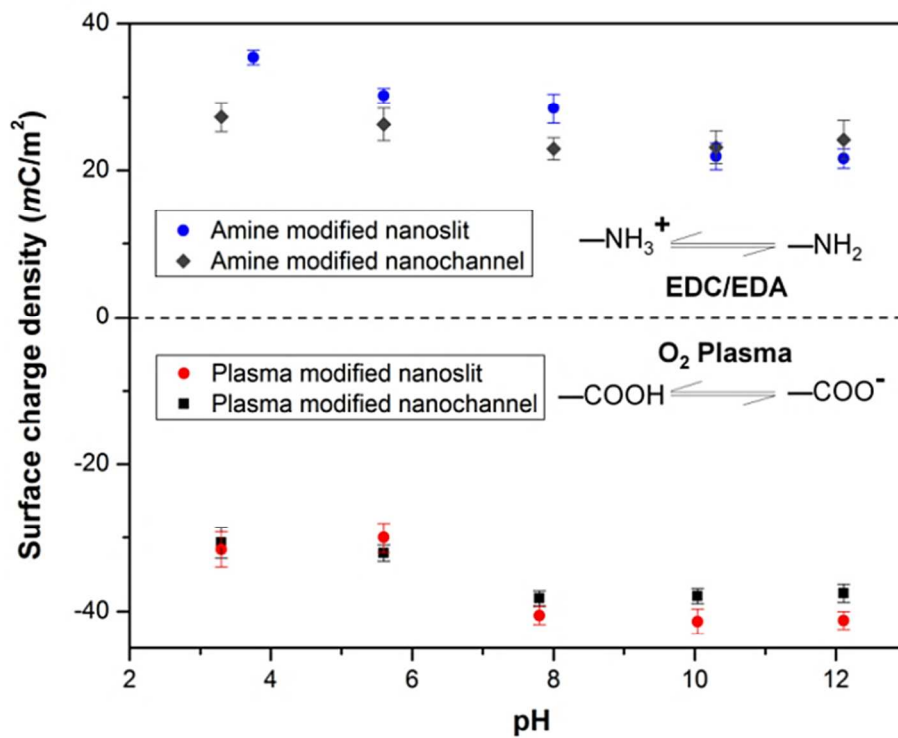
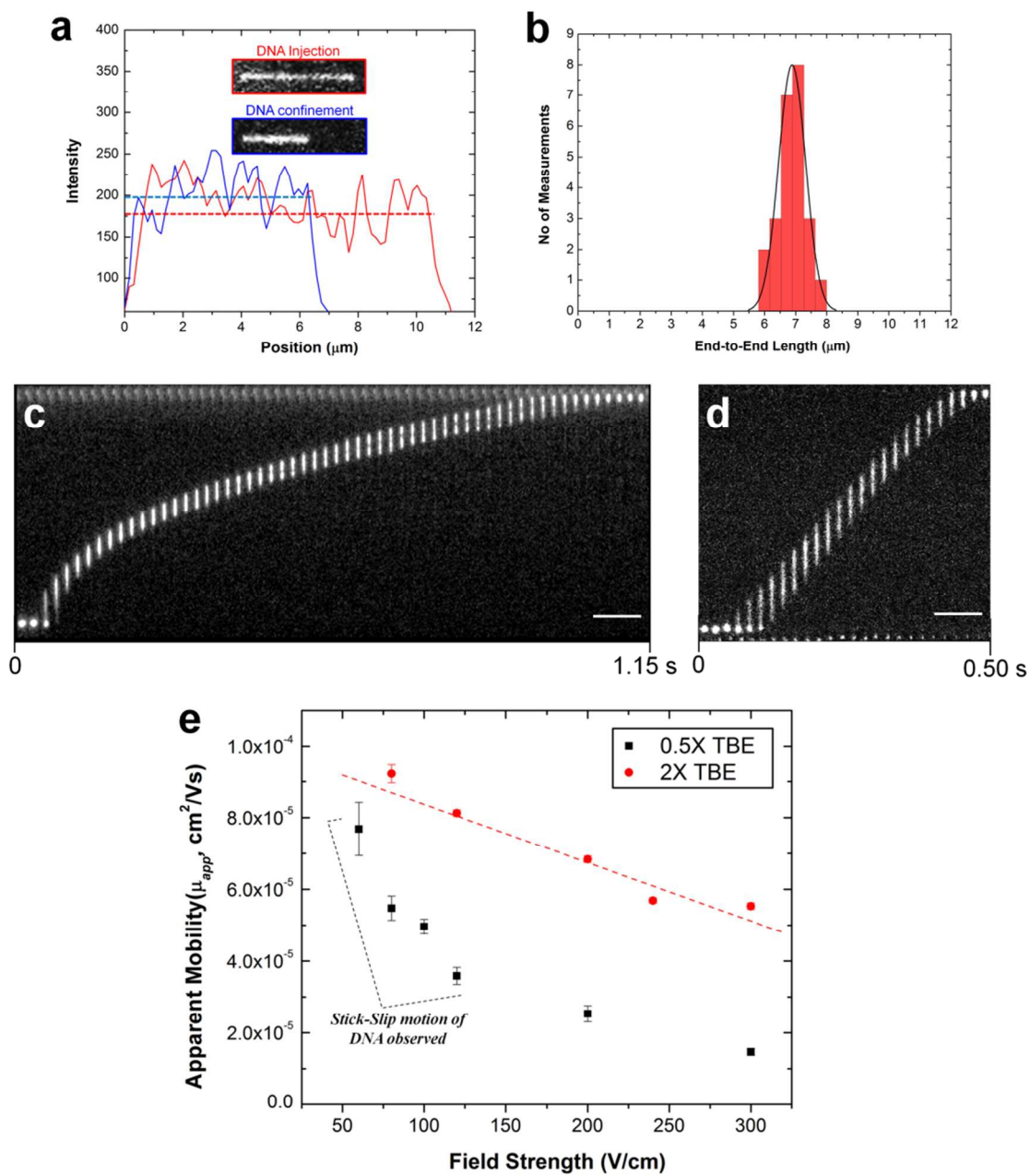


Figure 6.



## Graphical Table of Content

